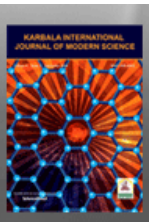
Karbala International Journal of Modern Science

Manuscript 3431

Synthesis and Characterization of Fe-Zn Bimetallic Nanoparticles via Two-Step Laser Ablation and Their Antibacterial Activity

Hudhaifa M. Mohammed

Sahar Naji Rashid

Synthesis and Characterization of Fe-Zn Bimetallic Nanoparticles via Two-Step Laser Ablation and Their Antibacterial Activity

Abstract

In this study, Nd: YAG laser at a wavelength of (1064 nm), energies of (300 and 400 mJ), and a pulse repetition rate of (3 Hz) was used to synthesize metallic nanoparticles from iron and zinc individually using a one-step pulsed laser ablation approach, followed by the two-step synthesis of bimetallic nanoparticles. The physical properties of the synthesized nanoparticles were then investigated using UV-visible (UV-Vis), X-ray diffraction (XRD), field-emission scanning electron microscopy (FESEM), and energy-dispersive X-ray (EDX) techniques. The results of characterization of the obtained NPs confirmed the formation of core-shell nanocomposites, as evidenced by the increased absorbance intensity of these samples, resulting from increased size averages and surface roughness, in addition to the formation of the Fe_2O_4Zn nanocomposite resulting from the two-step ablation process. The increased absorbance and size of the nanoparticles suggest an enhanced interaction with light, which could be advantageous for applications requiring strong optical properties. UV-Vis analysis showed that the ablation energy (400 mJ) resulted in higher absorption intensity for all samples and that the absorption intensity of the core-shell nanoparticles was the highest in comparison. The energy gap values generally ranged within the range (3.2 – 3.4 eV). XRD results revealed a polycrystalline structure with a hexagonal phase for both iron oxide nanoparticles and zinc oxide nanoparticles, the average crystalline sizes (59.6 nm) and (73.1 nm), respectively, and a cubic phase for the bimetallic (core-shell) nanocomposites, with increased average sizes of (85.2 nm) and (82.12 nm). FESEM results showed rough surfaces for these nanoparticles, as well as the presence of clusters and agglomerates, with an average size within the nanoscale range (90 nm). This increase in size, in turn, led to increased absorption compared to iron oxide and zinc oxide nanoparticles. The nanoscale of the synthesized nanoparticles led to their antibacterial activity, as all synthesized nanoparticles showed an effect on two types of bacteria, one Gram-positive and the other Gram-negative, where the inhibition ranges ranged within the range (12 – 18 mm), which indicates that the structural and optical properties of the core-shell nanocomposites may contribute to their effectiveness as potential alternatives to traditional antibiotics to inhibit bacteria.

Keywords

Antibacterial effectiveness; Core-shell nanoparticles; Nano-colloidal; Nanocomposite; Laser energy

RESEARCH PAPER

Synthesis and Characterization of Fe-Zn Bimetallic Nanoparticles via Two-step Laser Ablation and Their Antibacterial Activity

Hudhaifa M. Mohammed, Sahar N. Rashid*

Department of Physics, College of Science, University of Tikrit, Tikrit, Iraq

Abstract

In this study, Nd: YAG laser at a wavelength of (1064 nm), energies of (300 and 400 mJ), and a pulse repetition rate of (3 Hz) was used to synthesize metallic nanoparticles from iron and zinc individually using a one-step pulsed laser ablation approach, followed by the two-step synthesis of bimetallic nanoparticles. The physical properties of the synthesized nanoparticles were then investigated using UV−visible (UV−Vis), X-ray diffraction (XRD), field-emission scanning electron microscopy (FESEM), and energy-dispersive X-ray (EDX) techniques. The results of characterization of the obtained NPs confirmed the formation of core-shell nanocomposites, as evidenced by the increased absorbance intensity of these samples, resulting from increased size averages and surface roughness, in addition to the formation of the Fe_2O_4Zn nanocomposite resulting from the two-step ablation process. The increased absorbance and size of the nanoparticles suggest an enhanced interaction with light, which could be advantageous for applications requiring strong optical properties. UV−Vis analysis showed that the ablation energy (400 mJ) resulted in higher absorption intensity for all samples and that the absorption intensity of the core-shell nanoparticles was the highest in comparison. The energy gap values generally ranged within the range (3.2−3.4 eV). XRD results revealed a polycrystalline structure with a hexagonal phase for both iron oxide nanoparticles and zinc oxide nanoparticles, the average crystalline sizes (59.6 nm) and (73.1 nm), respectively, and a cubic phase for the bimetallic (core-shell) nanocomposites, with increased average sizes of (85.2 nm) and (82.12 nm). FESEM results showed rough surfaces for these nanoparticles, as well as the presence of clusters and agglomerates, with an average size within the nanoscale range (90 nm). This increase in size, in turn, led to increased absorption compared to iron oxide and zinc oxide nanoparticles. The nanoscale of the synthesized nanoparticles led to their antibacterial activity, as all synthesized nanoparticles showed an effect on two types of bacteria, one Gram-positive and the other Gram-negative, where the inhibition ranges ranged within the range (12−18 mm), which indicates that the structural and optical properties of the core-shell nanocomposites may contribute to their effectiveness as potential alternatives to traditional antibiotics to inhibit bacteria.

Keywords: Antibacterial effectiveness, Core-shell nanoparticles, Nano-colloidal, Nanocomposite, Laser energy

1. Introduction

Currently, many types of pharmaceutical compounds and antibiotics are used in large quantities worldwide as treatments for microbial infections. However, the growing demand for these treatments and their overuse have led to the emergence of drug resistance in bacteria through self-evolution, leading to a gradual loss of effectiveness and the emergence of numerous uncommon health problems that cause environmental pollution. Therefore, the need to develop effective antibacterial alternatives to antibiotics has arisen. Researchers are turning to nanotechnology as a promising solution [1,2]. Nanotechnology is considered one of the most important fields in various sciences (physics, chemistry, and biology). Materials that can be produced in sizes ranging

Received 28 May 2025; revised 24 August 2025; accepted 28 August 2025.
Available online 26 September 2025

* Corresponding author.
E-mail address: sahar83@tu.edu.iq (S.N. Rashid).

https://doi.org/10.33640/2405-609X.3431

from 1 to 100 nm are known as nanomaterials, which are distinct and unique materials. The science that is concerned with studying and describing these materials and determining their physical and chemical properties is nanoscience [3,4]. When materials are transformed to very small sizes, within the nanoscale range, they acquire characteristics, properties, and chemical, biological, or physical properties that are completely different from their larger-sized counterparts. These new and distinctive properties have a direct impact on their chemical reactions and stability, and increase their surface area relative to their volume [3]. Therefore, there are many important and growing applications for this field [5]. This involves the usage of nanoparticles (NPs) in the medical field to develop various treatments for diseases that may affect humans. Several treatments have been developed, particularly for cancer and some infectious diseases, using metallic NPs. These NPs are used to deliver drugs to affected areas due to their large surface area relative to their size [2,6]. They are mainly used as heterogeneous nanocatalysts in a variety of organic transformations. This is due to their high surface area and small sizes, which impact specific biological and catalytic applications [7]. NPs can be prepared in many ways, whether chemically, physically, or biologically. Each method has its own characteristics that distinguish it from the rest. There are two basic types of strategies for preparing NPs. The first method is top-down, which is based on breaking the material through the effect of an external force on solid materials. This process reduces the material to very small particles. The second method is the cumulative approach, or bottom-up, in which individual atoms are built one by one to form molecules [8,9]. PLAL (pulsed laser ablation in liquids) is a technique that represents one of the simplest and most versatile methods for synthesizing NPs [10]. It is a simple and rapid process to synthesize NPs of pure metals and metal oxides with uniformity and minimal aggregation, and it is a non-toxic and non-polluting method [11,12]. It is also low-cost and highly effective. It is a physical method for preparing nanomaterials using a top-down approach [13,14]. This is done by placing a piece of high-purity metal as a target in a liquid medium and exposing it to a pulsed laser beam to remove NPs from the target surface, mix them with the fluid medium, and form a colloidal solution containing a mixture of liquid and NPs. The ablation process is highly controlled, producing pure metal NPs and metal oxides without the need for catalysts or chemicals. The ablation parameters include the liquid medium, laser wavelength, laser transmittance, laser energy, laser beam focal length, laser pulse duration, laser shot count, and laser pulse repetition rate, where the shape and size of the NPs can be controlled by controlling the laser parameters. These parameters can be controlled to prepare NPs for various applications, such as solar cells, antibacterial activity, drug delivery, and more [15–17]. Recently, the core-shell NPs synthesis technique has gained great attention through the formation of bimetallic NPs, a prominent type of hybrid NPs that may contain organic or inorganic materials, such as metals. One material serves as the core, while the other material covers it, forming a shell. This nanostructure has enhanced and improved the multiple applications of nanomaterials, resulting in unique properties for the prepared NPs, most notably the enhancement of the structure, stability, and greater effectiveness, which makes them useful in several fields, most notably drug delivery and inhibition of bacteria and viruses [18–20]. The behavior of the core-shell composition is between that of the core and shell components, and this composite can form a structure with superior performance that overcomes the obstacles inherent in single-phase structures [21]. Nanocomposites (core-shell) are important in biomedical applications, especially when they have non-toxic behavior [22]. A significant amount of effort has been focused on nanocomposites. The advantages of combining metallic nanocrystals have to do with economic benefits, non-toxicity, and stable characteristics [23]. Based on a metallic precursor, two-step PLAL can form core-shell NPs with novel behavior and properties, which have the advantage of greater control over the size and surface modification of NPs [21]. It is one of the best methods used to produce composite nanomaterials, which relies on the use of a variety of laser parameters and the media surrounding the target, which affects the size, shape, and structure of the resulting material. This strategy can produce composite nanomaterials containing semiconductor materials. This method relies heavily on the use of short, high-intensity pulses, up to nanoseconds, using a high-power laser source, producing small objects with special properties in the nanoscale state [24]. Zinc oxide nanoparticles (ZnO NPs) have unique optical and structural properties, and when they reach the nanoscale, this affects their mechanical, electrical, and morphological properties. Among their most prominent applications are optical coatings, solar cells, and antibacterial, as they replace antibiotics and deliver medicine to infected areas [25]. Iron oxide nanoparticles (FeO NPs) are characterized by their high magnetism and low

toxicity, which enables them to be used on a wide scale, most notably in nanomedicine, by delivering treatment to infected areas, as well as being an effective antibacterial and antiviral, which have recently begun to show high resistance to conventional antibiotics [16]. So, these two types of NPs are the subject of the current study for their distinctive properties. Although there are many previous studies on the synthesis of core-shell nanocomposites in several ways, as mentioned above, characterizing them using different techniques, and evaluating their biological effectiveness, what distinguishes the current study is the possibility of considering it a sustainable synthesis of core-shell NPs without affecting the environment, and in a rapid manner that saves time and effort, and from two materials that are friendly to the human body (Fe and Zn) when compared to other materials with toxicity concerns, even if it is in the long run. In addition, this study tested the effectiveness of the synthesized nanoparticles against two different types of bacteria. With the increasing resistance of harmful bacteria in humans to many antibiotics, it has become necessary to find alternatives to reduce their resistance. One of the most prominent solutions on which our study was based and aimed is the use of transition metal NPs to reduce resistance, especially since preparation via a sustainable method, namely pulsed laser ablation in deionized water, as this method is non-toxic and does not require harmful chemicals. Iron and zinc oxide NPs were synthesized using two different laser energy levels, in addition to synthesizing a core-shell nanocomposite of these two metals to improve the resulting properties and effectiveness of the resulting NPs. The effectiveness of all synthesized NPs was tested on two types of bacteria to verify their inhibition effectiveness.

2. Materials and methods

2.1. NPs synthesize

Two metals, Fe and Zn, with a purity for each other of (99.9 %) from Laboratory Chemical-India, were used in this study to synthesize metallic NPs and then bimetallic NPs by the two-step PLAL technique.

To synthesize NPs from Fe metal, the Fe sheet with dimensions (2 × 2 × 0.1 cm) was immersed in (5 mL) of the deionized water (DW), in a (100 ml) glass beaker, at a distance of (10 cm) from the Q-switched Nd: YAG laser source with (700 pulses), a repetition pulses rate of (3 Hz), a wavelength of (1064 nm), the liquid level was (7 mm) above the target, and two different energies of (300 and 400 mJ). As well to synthesize NPs from Zn metal, the Zn sheet with dimensions (2 × 2 × 0.1 cm) was immersed in (5 mL) of DW, in a (100 ml) glass beaker, at a distance of (10 cm) from the laser source with (300 pulses), a repetition pulses rate of (3 Hz), a wavelength of (1064 nm), the liquid level was (7 mm) above the target, and two different energies of (300 and 400 mJ). Nano-colloidal solutions were prepared for each metal separately. The laser parameters for ablation were determined and selected based on laboratory experimental steps, starting with the first harmonic of the wavelength, the lowest energies, and the pulse repetition rate to save time, effort, and energy, provided that these parameters are productive for nanoparticles.

In synthesizing the (Fe@Zn) core-shell NPs, the Fe sheet was immersed in the colloidal solution containing the prepared NPs of Zn metal (shell). Then, the NPs (core) were ablated from it by applying the same ablation parameters used in the NPs synthesizing NPs from Fe metal. In synthesizing the (Zn@Fe) core-shell NPs, the Zn sheet was immersed in the colloidal solution containing the prepared NPs from Fe metal (shell). Then, the NPs (core) were ablated from it by applying the same ablation parameters used in the synthesis of NPs from Zn metal. For all prepared samples, the laser spot diameter on the target was 1 cm, while the laser fluence when using ablation energy (300 mJ) and (400 mJ) was (0.38 J/cm^2) and (0.51 J/cm^2), respectively. Thus, (8) samples of nano-colloidal solutions were obtained: two samples representing the colloidal solution containing NPs from Fe metal prepared with two laser energies (300 and 400 nm), two samples representing the colloidal solution containing NPs from Zn metal prepared with the two energies, two samples representing the colloidal solution containing (Fe@Zn)NPs prepared with the two energies, and two samples representing the colloidal solution containing (Zn@Fe)NPs prepared with the two energies.

2.2. NPs characterization

The prepared samples were characterized optically and structurally, where the absorption spectrum of all prepared samples was found using the UV–visible (UV–Vis) spectrophotometer, from Metertech Inc., after their preparation was completed, and their energy gap (Eg) was calculated using Eq. (1) [26,27]:

$$\alpha h\upsilon = B(h\upsilon - Eg)^{1/2} \quad (1)$$

Where α is the absorption coefficient, h represents the Planck constant, υ represents the photon frequency, and B is a constant. The structural characterization was also obtained using X-ray diffraction (XRD), from Haoyuan Instrument, to determine the sample's constituent elements by finding Bragg diffraction angles and Miller indices. The phases and crystal size averages were also determined using the Debye-Scherrer Eq. (2) [28,29], the distances between crystal planes, and the full width at half maximum (FWHM) of the diffraction peaks.

$$D = K\lambda / \beta \cos\theta \quad (2)$$

Where K is constant, λ is the wavelength of the X-ray, β represents FWHM, and θ is the Bragg diffraction angle. The second technique used for structural characterization is the field-emission scanning electron microscopy (FESEM), from InspectTM F50, to determine the surface morphology, shapes, and diameter averages of the synthesized NPs. This technique also provides another associated technique, namely energy-dispersive X-ray spectroscopy (EDX), which is useful in determining the percentage and weight ratios of the elements composing the prepared samples.

3. Biological application

The agar diffusion method was used to evaluate the effectiveness of all the prepared nano-colloidal solutions on the two types of bacteria, one of which was Gram-positive, *Staphylococcus aureus* (*S. aureus*), and the other Gram-negative, *Escherichia coli* (*E. coli*), isolated from the urinary tract. The inhibition was tested using the agar diffusion method, where bacterial cells were spread using a cotton swab on Mueller-Hinton agar medium in Petri dishes. Holes were then made in these dishes to place the prepared nano-colloidal solutions in them, and then incubated for (24 h) at a temperature of (37 °C) where the sensitivity of the two bacterial strains to the NPs was evaluated through the inhibition zone that appeared on the agar plate around the hole [30]. The effectiveness of all prepared samples was tested on the two types of bacteria used.

Fig. 1 shows a simplified diagram of the details of this study.

4. Results and discussion

4.1. UV–Vis analysis

Optical characterization of the ablated Fe and Zn nanoparticles for all the prepared samples was performed using the UV–Vis spectrophotometer, and the absorption spectra shown in Figs. 2–4 were obtained. The results demonstrate that the absorbance increases with increasing laser energy in the ablation process. Fig. 2 shows the absorption spectra of NPs ablated from Fe metal, showing that the sample synthesized at (400 mJ) has an absorbance intensity higher than that of the sample synthesized at (300 mJ). The absorbance peak represents the surface plasmon resonance (SPR) of the Fe nanoparticles, a characteristic feature of transition element NPs that represents the collective oscillation of the free electrons in these particles when light is incident on them. This phenomenon occurs at the interface between the metal and the insulator (liquid medium). When polarized light falls on this interface at a certain angle, it excites the free electrons on the metal surface, causing collective vibrations (surface plasmons). This value is affected by the concentration of the solution [31]. Fig. 3 shows the two absorbance spectra of NPs

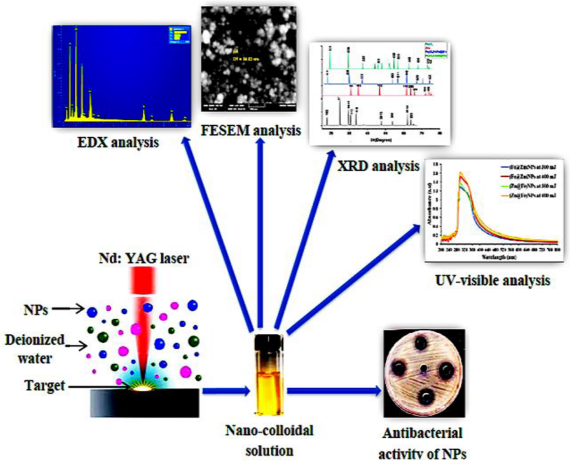

Fig. 1. Simplified outline of the current study.

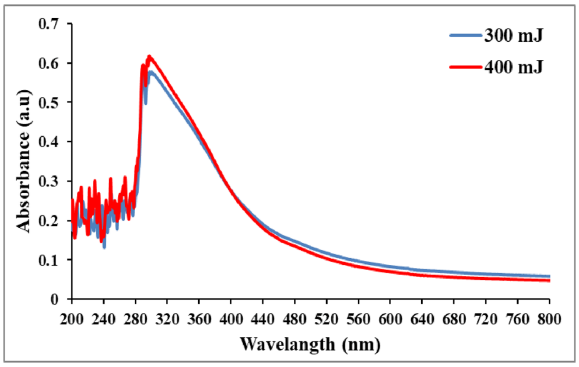

Fig. 2. Absorbance spectra of NPs ablated from Fe.

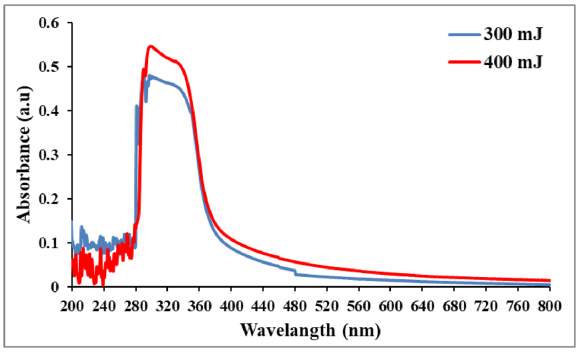

Fig. 3. Absorbance spectra of NPs ablated from Zn.

ablated from Zn metal. The maximum absorbance that represents the SPR of the Zn nanoparticles was (400 mJ). In comparison, the absorbance of iron-ablated NPs is higher than that of zinc-ablated NPs. The results showed that the SPR of the Fe-ablated NPs is higher than that of the Zn-ablated ones, as it was found that the surface plasmon excitation efficiency of Fe is higher. This is due to the dependence of this phenomenon on the optical and magnetic properties of the materials. It is also affected by the valence number of the material. As a result, the Fe-ablated NPs show a higher plasmon resonance efficiency [32]. Fig. 4 shows the absorbance spectrum of both the resulting composite (Fe@Zn) core-shell and (Zn@Fe) core-shell NPs. The higher ablation energy (400 mJ) led to the formation of core-shell nanocomposites with higher absorption intensity. It can be noted that the (Zn@Fe)NPs synthesized with both ablation energies showed higher absorption compared to the (Fe@Zn)NPs. This is due to the effect of the nano-colloid solution of the Fe (shell) with higher absorption compared to the nano-colloid solution of the Zn (core). Also, the higher ablation energy led to a higher absorption intensity due to the increased concentration of nanoparticles in the nano-colloidal solutions. The higher SPR peak of the nano-colloid solutions produced by the two-step ablation process is one of the pieces of evidence for the formation of core-shell nanocomposites [20,33].

These results demonstrate that increasing the ablation energy leads to an increase in the number of NPs and, consequently, an increase in the concentration of the nano-colloidal solution. The difference in the peak and width of the absorption spectra resulting from the use of the two energies may indicate that increasing the laser energy caused an increase in the concentration of the NPs formed, a change in their size or shape, or the formation of crystalline defects that affect the absorption properties. The results show that the absorbance of the core-shell NPs is significantly higher than that of both Fe and Zn nanoparticles, proving their efficiency.

The peak (SPR) of all synthesized NPs ranged around the wavelength (300 nm), and there was a difference in their intensity and broadness, as the higher absorption intensity indicates an increase in the size of the resulting NPs with increasing energy, which led to higher absorption efficiency. As for the increase in the broadness of the peak with increasing energy, it indicates the occurrence of dispersion in shape and size, as the optical properties of the material depend on its structural properties. We also note an increase in the SPR intensity value for the core-shell nanocomposites, as this value is affected by the refractive index of the medium, as the synthesis process of these nanocomposites was carried out in two steps, using a nano colloidal solution of the material as a liquid medium for ablation, and this means a change in the refractive indices [31]. Figs. 5–8 represent the results of calculating the energy gap (Eg) for all prepared nanoparticles. Fig. 5 shows the Eg results for Fe oxide NPs. At (300 mJ), Eg was (3.25 eV),

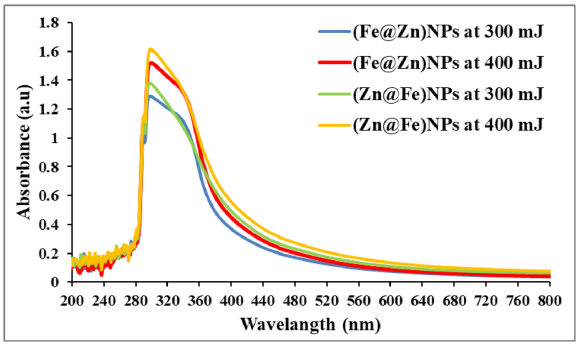

Fig. 4. Absorbance spectra of (Fe@Zn) and (Zn@Fe) core-shells NPs.

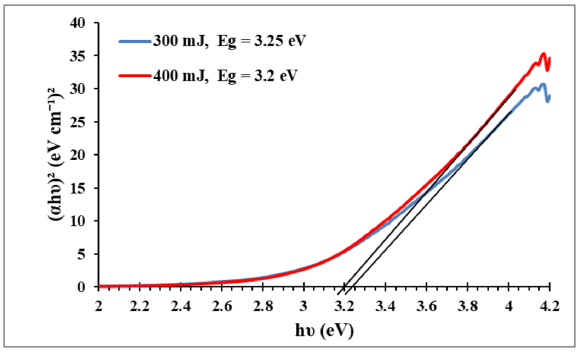

Fig. 5. Energy gap of Fe oxide NPs.

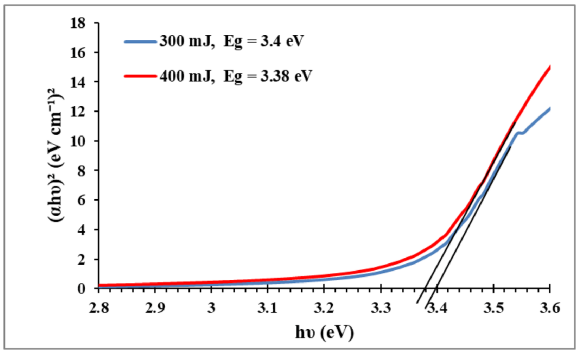

Fig. 6. Energy gap of Zn oxide NPs.

while at (400 mJ), it was (3.2 eV). Fig. 6 shows the Eg results for Zn oxide NPs. At (300 mJ), Eg was (3.4 eV), while at (400 mJ), it was (3.38 eV). As for the core-shell composites, Fig. 7 shows Eg values for (Fe@Zn)NPs. At (300 mJ), Eg was (3.32 eV), while at (400 mJ), it was (3.3 eV). Fig. 8 shows the results of Eg for the second core-shell composite (Zn@Fe) NPs. At (300 mJ), the value was (3.22 eV), while at (400 mJ), it was (3.3 eV). The Eg values of the prepared samples are inversely proportional to the increase in energy. The higher the ablation energy, the smaller Eg. This facilitates the transition of electrons from the valence band to the conduction band, significantly increasing the sample's conductivity. This slight change in the energy gap may indicate a slight modification in the electronic structure of the material due to changes in the preparation conditions. The result of the decrease in the energy gap value with the increase in absorbance is consistent with previous studies such as [33–36].

4.2. XRD analysis

Fig. 9 represents XRD patterns obtained from the samples prepared at the ablated energy (400 mJ). The results denote that the process of ablation of Fe metal at the working conditions led to the formation of Fe_2O_3 NPs with a hexagonal crystal structure, where the peaks appeared consistent with the standards of the international card (JCPDS) card number (00-040-1139), and the average crystalline size (59.6 nm). The results also show that the process of ablation of Zn metal led to the ZnO nanoparticles, which also have a hexagonal crystal structure, where the peaks show consistency with the JCPDS card number (01-075-1533). And the average crystalline size was (73.1 nm). As for the two composites (core-shell) synthesized at both (Fe@Zn) and (Zn@Fe), the results showed that the formation of Fe_2O_4Zn NPs with the cubic crystals phase shows good agreement with the JCDPS card number (01-081-0676), the average crystalline sizes of these two composite NPs synthesized from Fe@Zn and Zn@Fe were (85.2 nm) and (82.12 nm) respectively. The crystalline size of the samples, shown in Table 1, was found using Eq. (2). A slight difference appeared in the diffraction patterns of the two nanocomposites (Fe@Zn) and (Zn@Fe) in terms of the intensity of the diffraction peaks, their broadness, the slight shifts, and the inter-spaces, which consequently led to a difference in the average crystal sizes of these two nanocomposites. The reason may be due to the difference in crystal stresses and compressive pressure on the core and shell in the two cases, and perhaps structural phases may have formed at the interface, which causes this difference.

4.3. FESEM analysis

Figs. 10–13 represent the FESEM results of NPs synthesized at (400 mJ). The Figures show the shapes of the synthesized NPs on several scales. Fig. 10 shows the nanoparticles ablated from Fe metal, which appear in regular spherical shapes,

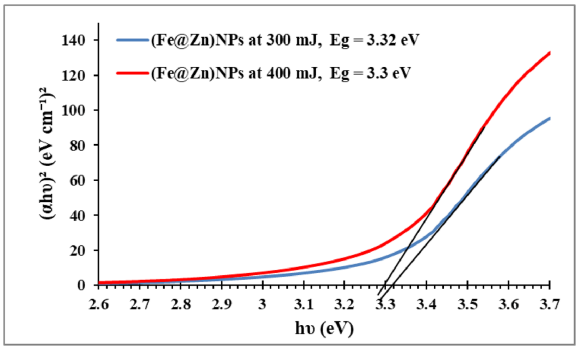

Fig. 7. Energy pap of (Fe@Zn) core-shells NPs.

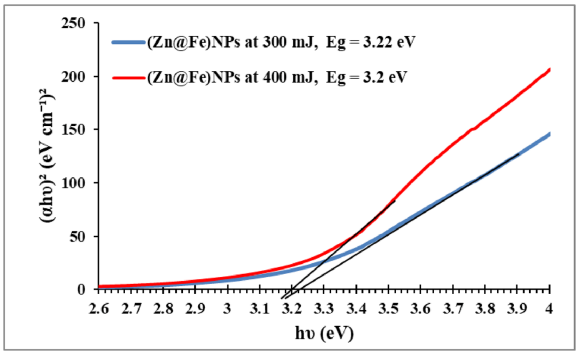

Fig. 8. Energy pap of (Zn@Fe) core-shells NPs.

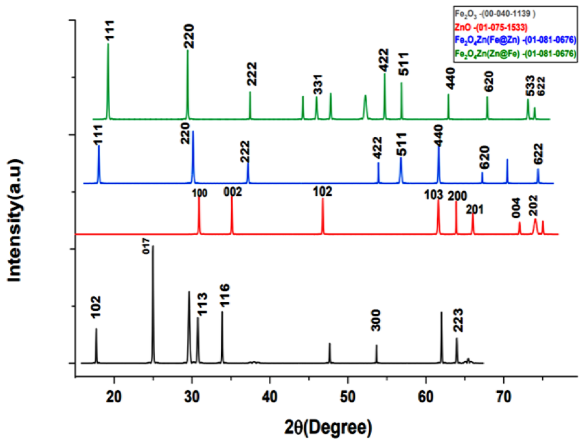

Fig. 9. XRD patterns of the synthesized samples.

especially in the figure on the scale (100 nm), and their average size (39.7 nm). While Fig. 11 shows the NPs ablated from Zn metal, they appear in irregular shapes and sometimes in the form of clustered sheets, especially on a scale of (500 nm) and with an average size of (67.5 nm). The irregularity in the size distribution of these NPs compared to that of NPs synthesized from Fe metal was reflected in the absorption spectrum, which appeared more regular and smooth. The average sizes of the core-shell NPs were (69 nm) and (90 nm) for Fe@Zn in Fig. 12 and Zn@Fe in Fig. 13, respectively. The NPs formed here appear to be clustered and agglomerated as a result of the superposition of the two types of NPs of the two metals, where one of them coats the other. The average sizes were calculated using the ImageJ program. These clusters and agglomerations lead to irregular shapes, despite being within the nanoscale. This is evident from the size distributions in the mentioned Figures. The size distributions of NPs and the resulting average sizes indicate that the core-shell nanocomposites showed a difference in these distributions and an increase in the average size, in addition to an increase in roughness as shown by the surface morphology. In general, the appearance of NPs clusters and agglomerations is due to several reasons, including van der Waals forces and a high surface area ratio, which makes them chemically unstable and prone to bonding with other particles, instability, and dispersion, especially when they are present in a liquid and without using a stabilizer. Also, the change in temperature affects the surface charge,

Table 1. XRD results parameters of the synthesized NPs.

Metal	NPs	2θ (deg)	hkl	β (rad)	d (nm)	D (nm)
Fe	Fe_2O_3	17.710	102	0.476	4.998	16.478
		24.978	017	0.109	3.559	70.657
		30.750	113	0.168	2.903	45.482
		33.855	116	0.105	2.644	71.976
		53.664	300	0.069	1.706	102.401
		63.979	223	0.133	1.454	50.542
Zn	ZnO	30.911	100	0.111	2.889	74.153
		35.109	002	0.105	2.570	78.926
		46.785	102	0.105	1.940	81.726
		61.605	103	0.172	1.502	53.453
		63.908	200	0.072	1.455	68.309
		66.042	201	0.138	1.413	72.677
		72.034	004	0.365	1.310	72.6773
		74.061	202	0.121	1.279	82.5991
Fe@Zn	Fe_2O_4Zn	18.031	111	0.139	4.908	57.7624
		30.132	220	0.145	2.962	56.4322
		37.177	222	0.131	2.415	63.6115
		53.919	422	0.070	1.699	125.803
		56.809	333	0.200	1.619	45.0212
		61.644	440	0.140	1.503	65.6206
		67.260	442	0.071	1.391	133.578
		70.444	620	0.071	1.336	136.471
		74.410	622	0.121	1.273	82.3526
Zn@Fe	Fe_2O_4Zn	19.222	111	0.140	4.607	57.2522
		29.435	220	0.109	3.030	75.0305
		37.445	222	0.069	2.399	120.872
		45.980	331	0.164	1.972	52.5614
		52.241	422	0.304	1.749	29.0183
		56.905	511	0.071	1.617	125.814
		62.899	440	0.071	1.476	130.831
		67.886	620	0.103	1.379	92.2732
		73.119	533	0.163	1.293	60.4125
		73.963	622	0.128	1.280	77.0923

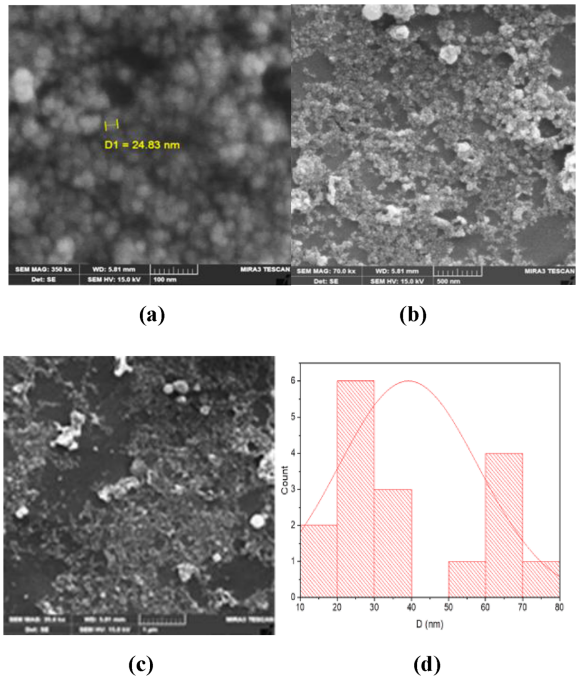

Fig. 10. FESEM analysis of NPs ablated from Fe metal: (a) at 100 nm scale, (b) at 500 nm scale, (c) at 1 μm scale, (d) NPs size distribution.

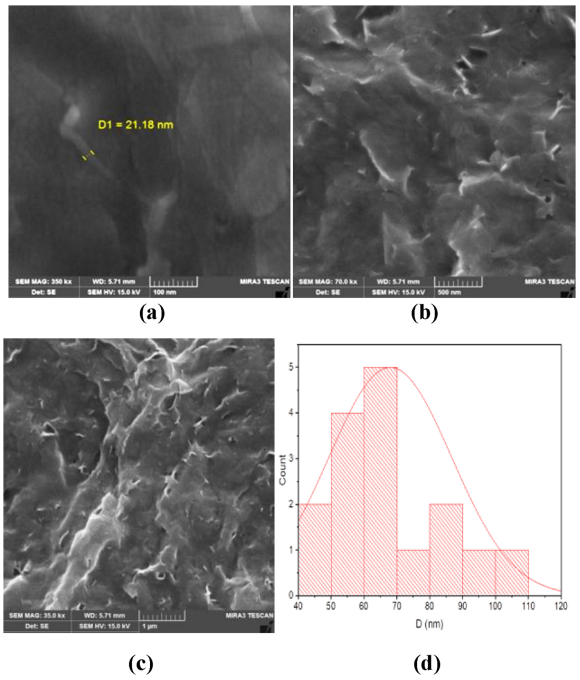

Fig. 11. FESEM analysis of NPs ablated from Zn: (a) at 100 nm scale, (b) at 500 nm scale, (c) at 1 μm scale, (d) NPs size distribution.

which leads to instability, dispersion, and agglomeration. Also, the evaporation of the liquid medium, especially during the test process, leads to the convergence of these particles and thus their agglomeration. As well as over time, as a result of the high surface energy of the smaller NPs, they settle onto the relatively large NPs, which leads to the growth of large NPs at the expense of the small ones, resulting in inhomogeneous dispersion [37,38].

4.4. EDX analysis

Figs. 14–17 show the results of the EDX analysis of the NPs synthesized at (400 mJ). The results indicate that all samples contain oxygen as a result of the oxidation of the samples since the ablation process took place in the air, and that the laser energy with the resulting heating of the metal during the ablation process and the formation of plasma led to a difference in the molecular pressures and the formation of oxides of these metals. This is in addition to the fact that these two elements tend to oxidize greatly by nature, and this is what appeared from the agreement of the diffraction peaks appearing in the XRD patterns and their agreement with the standard cards for the oxides of these elements. The emergence of additional peaks in the EDX spectra of the two-step synthesized nanoparticles indicates the formation of core-shell nanocomposites, especially as it is coupled with FESEM. The appearance of inaccurate and unclear EDX images is due to several factors related to the

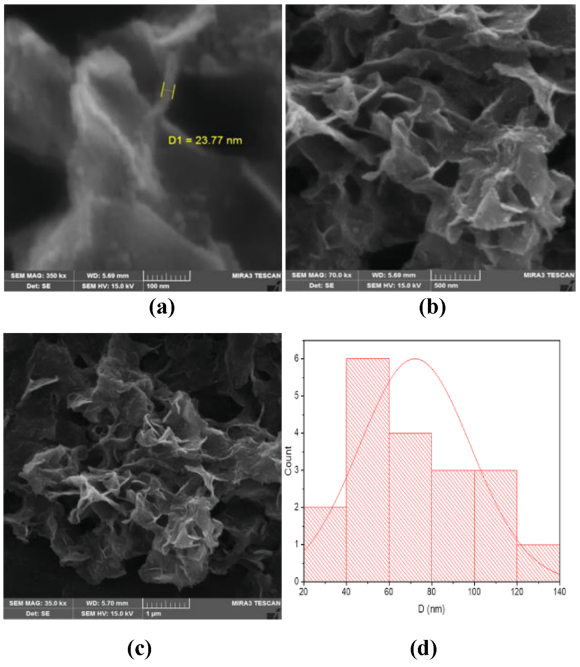

Fig. 12. FESEM analysis of (Fe@Zn)NPs: (a) at 100 nm scale, (b) at 500 nm scale, (c) at 1 μm scale, (d) NPs size distribution.

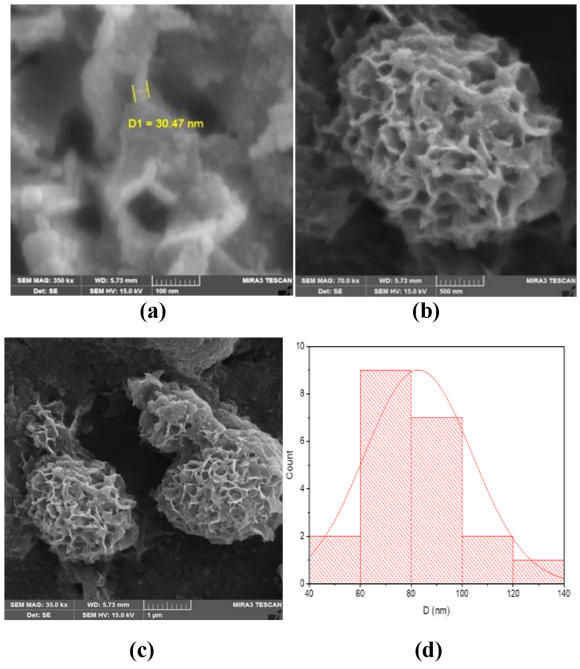

Fig. 13. FESEM analysis of (Zn@Fe)NPs: (a) at 100 nm scale, (b) at 500 nm scale, (c) at 1 μm scale, (d) NPs size distribution.

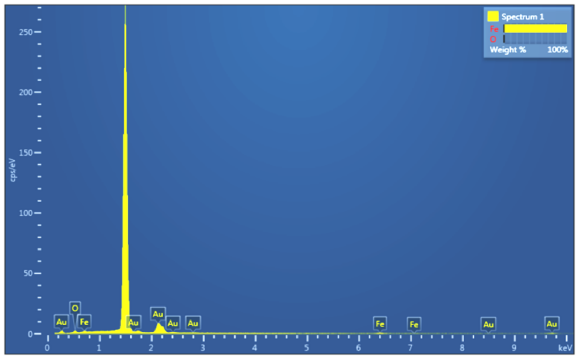

Fig. 14. EDX analysis of NPs ablated from Fe metal.

measuring device itself, including surface thickness inhomogeneity, electron scattering by air molecules, and possible contamination. High electron beam current, inappropriate acceleration voltage, analysis time, the type of detector used, and other factors also affect the quality of the analysis images. Other causes of inaccurate and unclear images include improper data processing or the use of inaccurate analysis algorithms. The appearance of the gold (Au) element specifically is due to the coating of the base of the EDX device with a thin layer of Au to improve electrical conductivity.

The results of characterization of the obtained NPs confirmed the formation of core-shell nanocomposites, as evidenced by the increased absorbance intensity of these samples, resulting from increased size averages and surface roughness, in addition to the formation of the Fe_2O_4Zn nanocomposite resulting from the two-step ablation process. The optical, structural, and morphological characterization results were consistent with each other. XRD results confirmed the formation of the aforementioned NPs, based on their compatibility with standard cards and the increased crystalline size averages of the core-shell nanocomposites. This, in turn, led to an increase in their size averages, according to the FESEM results. This was evident from the rougher morphology of the surfaces of these NPs, in addition to the appearance of clusters and agglomerations. This increase in size, in turn, led to an increase in their absorbance compared to the absorbance of Fe and Zn oxide NPs.

4.5. Antibacterial activity

All the prepared samples showed antibacterial effectiveness as very good inhibition zones with different diameters. Figs. 18 and 19 show the biological activity of NPs synthesized at (300 mJ) and (400 mJ), respectively, on *S. aureus* and *E. coli*. Fig. 20 illustrates the inhibition diameters of bacteria caused by the synthesized NPs.

All samples prepared using the ablation energy (400 mJ) showed a relatively greater inhibitory effect against the two types of bacteria used compared to those prepared using the energy (300 mJ), as the higher energy led to an increase in the ablated nanoparticles and thus their concentration in solution. This was evident from the absorption spectra. This increase in concentration led to a greater antibacterial effect for both types of bacteria. The effects of both the ablated iron and zinc nanoparticles individually and the bimetallic (core-shell) nanoparticles on the bacteria were generally similar, except for some variation in some samples, which proves the antibacterial effectiveness of all prepared nanoparticles. The results showed that the sensitivity of bacteria *E. coli* to the prepared nanoparticles, in general, was higher compared to bacteria *S. aureus* due to the difference in the bacterial cell wall nature. Upon reaching the surface of the bacterial cell, the prepared nanoparticles penetrate the bacterial cell membrane and cause damage by disrupting proteins and reducing cell permeability, leading to microbial death [39].

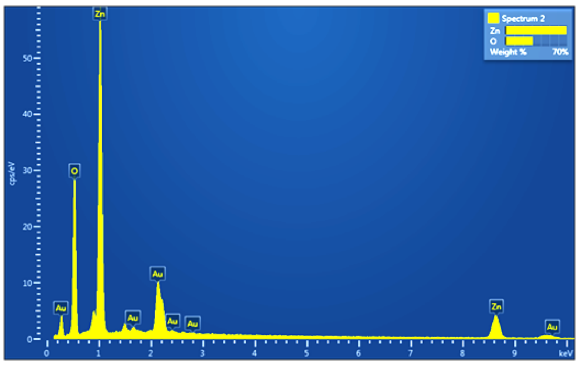

Fig. 15. EDX analysis of NPs ablated from Zn metal.

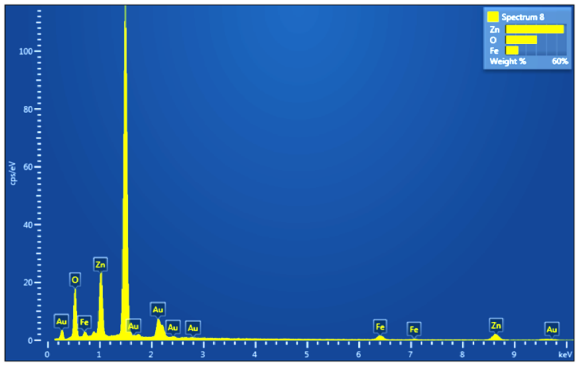

Fig. 16. EDX analysis of (Fe@Zn)NPs.

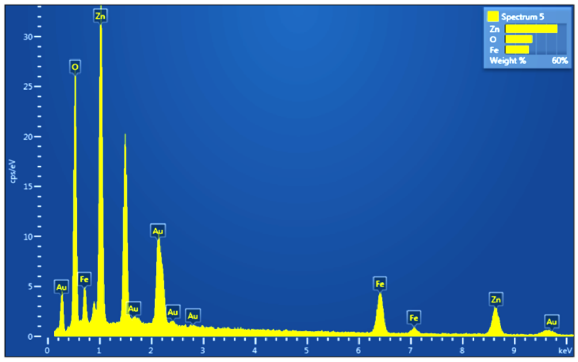

Fig. 17. EDX analysis of (Zn@Fe)NPs.

Experimental results indicated that the two types of bacteria differed in their sensitivity to nanoparticles. One possible explanation for this difference is the distinct composition of their cell walls. The effectiveness of nanoparticles is generally manifested by disrupting both the electron transport chain and energy transfer across bacterial membranes, which is their mechanism of action [40], leading to changes in cell membrane permeability. Researchers have hypothesized several possible mechanisms for the effect of nanoparticles on bacteria, including the formation of free radicals and the resulting weakening of the cytoplasmic membrane. In several previous studies, researchers have proposed several mechanisms to explain the behavior of nanoparticles against bacteria, including the production of reactive oxygen species (ROS), oxidative stress, adhesion to the cell membrane, and others that cause damage to the bacterial cell wall, thus nanoparticle penetration and cell death due to damage to mitochondria and DNA, and then cell death due to the cytotoxicity of nanoparticles [41]. The presence of NPs ablated

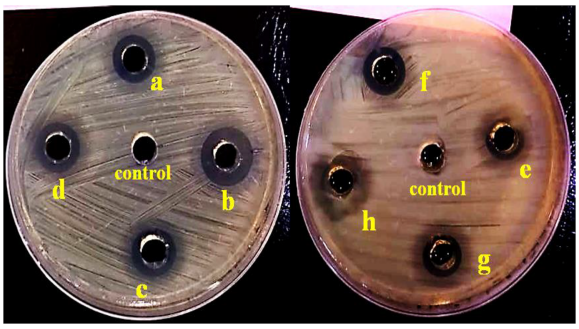

Fig. 18. S. aureus inhibition zone by the following samples: (a) NPs ablated from Fe at 300 mJ, (b) NPs ablated from Fe at 400 mJ, (c) NPs ablated from Zn at 300 mJ, (d) NPs ablated from Zn at 400 mJ, (e) Fe@Zn NPs at 300 mJ, (f) Fe@Zn NPs at 300 mJ, Fe@Zn NPs at 400 mJ, (g) Zn@Fe NPs at 300 mJ, (h) Zn@Fe NPs at 400 mJ.

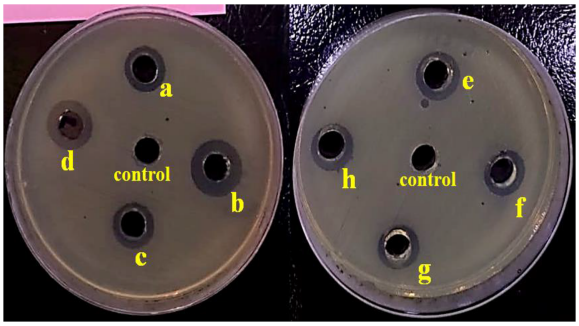

Fig. 19. E. coli inhibition zone by the following samples: (a) NPs ablated from Fe at 300 mJ, (b) NPs ablated from Fe at 400 mJ, (c) NPs ablated from Zn at 300 mJ, (d) NPs ablated from Zn at 400 mJ, (e) Fe@Zn NPs at 300 mJ, (f) Fe@Zn NPs at 300 mJ, Fe@Zn NPs at 400 mJ, (g) Zn@Fe NPs at 300 mJ, (h) Zn@Fe NPs at 400 mJ.

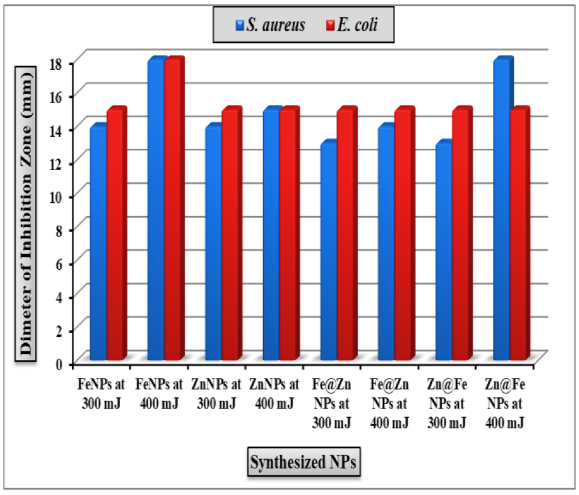

Fig. 20. Diagram of bacterial inhibition zone diameters.

from Fe metal enhances the generation of ROS and increases the stability of the particles in biological media [42]. On the other hand, the properties of the prepared nanoparticles, such as the small size of both crystals and nanoparticles on the one hand and the formation of clusters and agglomerations that lead to increased sizes on the other, affect the extent of their effectiveness against bacteria.

5. Conclusions

Pulsed laser ablation technology enables the easy, time-saving, and low-cost synthesis of monometallic and bimetallic nanoparticles. It produces no environmental impact compared to other methods. Characterization results showed that the core-shell nanocomposites had larger average sizes and higher surface roughness. This resulted in high absorption densities, especially at higher laser

fluences. Furthermore, incorporating nanoparticles of two metals led to a different crystalline phase in the bimetallic oxide nanocomposite. This was due to the two-stage ablation process. The synthesized core-shell nanoparticles exhibit good optical, structural, and morphological properties. They also show antibacterial activity, producing good diameter bacterial inhibition zones. This encourages further development and optimization. Controlling the ablation parameters can yield nanocomposites with higher inhibition efficiency. The key achievements of this work begin with the selection of two metals that have unique properties and are non-toxic and friendly to the human body. The nanoparticles were synthesized separately and in core-shell form using a sustainable and rapid technique. There is the ability to control the properties of the resulting nanoparticles by adjusting multiple ablation parameters and adapting them to the working environment and conditions. These products can also be used in several applications, particularly in human health. The antibacterial activity of the resulting nanoparticles against two types of bacteria enhances their potential as an alternative to antibiotics. They can be tested on other bacterial species or in other medical applications. Examples include use against fungi and cancer cells, and in various medical drugs such as wound dressings and various bioassays.

Ethics information

This study did not involve the use of animal or human subjects.

Funding

There is no funding for this research.

Conflicts of interest

The authors declare that they have no competing interests.

Acknowledgements

The authors thank the Physics Department at Science College in Tikrit University for providing the opportunity at the Optics and Laser Laboratory in the department to complete this work.

References

[1] S. Rauf, N. Safdar, Sustainable fabrication of biogenic Fe–Zn nano core-shell and their photocatalytic efficiency against third generation antibiotics, Mater. Chem. Phys. 313 (2024) 128784, https://doi.org/10.1016/j.matchemphys.2023.128784.

[2] S. Gavas, S. Quazi, T.M. Karpiński, Nanoparticles for cancer therapy: current progress and challenges, Nanoscale Res. Lett. 16 (2021) 173, https://doi.org/10.1186/s11671-021-03628-6.

[3] M.A. Kadhum, R.M. Abdullah, N. Yuseff, Preparation ZnO nanoparticles with different concentration by laser ablation in liquid and their use in antibacterial activity, Academic Sci. J. 2 (2024) 79–98, https://doi.org/10.24237/ASJ.02.01.835C. .

[4] Y. Khan, H. Sadia, S.Z.A. Shah, M.N. Khan, A.A. Shah, Naimat-Ullah, M. Farhat-Ullah, H. Bibi, O.T. Bafakeeh, N. Ben-Khedher, S.M. Eldin, B.M. Fadhl, M.I. Khan, Classification, synthetic, and characterization approaches to nanoparticles, and their applications in various fields of nanotechnology: a review, Catalysts 12 (2022) 1386, https://doi.org/10.3390/catal12111386.

[5] A. Haleem, M. Javaid, R.P. Singh, S. Rab, R. Suman, Applications of nanotechnology in medical field: a brief review, Global Health J. 7 (2023) 70–77, https://doi.org/10.1016/j.glohj.2023.02.008. .

[6] S. Anjum, M. Hashim, S.A. Malik, M. Khan, J.M. Lorenzo, B. H. Abbasi, C. Hano, Recent advances in zinc oxide nanoparticles (ZnO NPs) for cancer diagnosis, target drug delivery, and treatment, Cancers 13 (2021) 4570, https://doi.org/10.3390/cancers13184570.

[7] S.M.A. Aziz, U.M. Nayef, M. Rasheed, Synthesis of CuO@ZnO nanoparticle core–shell formed via laser ablation in liquid for photocatalytic applications, Plasmonics 20 (2025) 2595–2605, https://doi.org/10.1007/s11468-024-02488-x.

[8] M. Sajid, J.P. Wasylka, Nanoparticles: synthesis, characteristics, and applications in analytical and other sciences, Microchem. J. 154 (2020) 104623, https://doi.org/10.1016/j.microc.2020.104623.

[9] N. Abid, A.M. Khan, S. Shujait, K. Chaudhary, M. Ikram, M. Imran, J. Haider, M. Khan, Q. Khan, M. Maqbool, Synthesis of nanomaterials using various top-down and bottom-up approaches, influencing factors, advantages, and disadvantages: a review, Adv. Colloid Interface Sci. 300 (2022) 102597, https://doi.org/10.1016/j.cis.2021.102597.

[10] W. Norsyuhada, W. Mohd Shukri, H. Bakhtiar, S. Islam, N. Bidin, Synthesis and characterization of gold-silver nanoparticles in deionized water by pulsed laser ablation (PLAL) technique at different laser parameter, Int. J. Nanosci. 18 (2019) 1850015, https://doi.org/10.1142/S0219581X18500151.

[11] M.T. Elabbasy, M.F.H. Abd El-Kader, A.M. Ismail, A.A. Menazea, Regulating the function of bismuth (III) oxide nanoparticles scattered in chitosan/poly (vinyl pyrrolidone) by laser ablation on electrical conductivity characterization and antimicrobial activity, J. Mater. Res. Technol. 10 (2021) 1348–1354, https://doi.org/10.1016/j.jmrt.2020.12.109.

[12] H. Ali, A.M. Ismail, A.A. Menazea, Multifunctional Ag/ZnO/chitosan ternary bio-nanocomposites synthesized via laser ablation with enhanced optical, antibacterial, and catalytic characteristics, J. Water Proc. Eng. 29 (2022) 102940, https://doi.org/10.1016/j.jwpe.2022.102940.

[13] O. Gatsa, S. Tahir, M. Flimelová, F. Riahi, C. Doñate-Buendia, B. Gökce, A.V. Bulgakov, Unveiling fundamentals of multi-beam pulsed laser ablation in liquids toward scaling up nanoparticle production, Nanomaterials 14 (2024) 365, https://doi.org/10.3390/nano14040365.

[14] K. Novotný, I. Krempl, I. Afonin, L. Prokeš, P. Vaňhara, J. Havel, Laser-induced plasma spectroscopy in pulsed laser ablation synthesis of nanoparticles in liquid, Talanta 290 (2025) 127767, https://doi.org/10.1016/j.talanta.2025.127767.

[15] C.L. Pò, F. Ruffino, M.G. Grimaldi, S. Boscarino, Pulsed laser ablation in liquid: numerical evaluationof laser fluence, Physica Status Solidi (RRL) Rapid Res. Lett. Publ. Wiley-VCH GmbH 19 (2025) 2400348, https://doi.org/10.1002/pssr.202400348.

[16] R.A. Ismail, G.M. Sulaiman, S.A. Abdulrahman, T.R. Marzoog, Antibacterial activity of magnetic iron oxide

nanoparticles synthesized by laser ablation in liquid, Mater. Sci. Eng. C 53 (2015) 286–297, https://doi.org/10.1016/j.msec.2015.04.047. .
[17] A.H. Attallah, F.S. Abdulwahid, Y.A. Ali, A.J. Haider, Effect of liquid and laser parameters on fabrication of nanoparticles via pulsed laser ablation in liquid with their applications: a review, Plasmonics 18 (2023) 1307–1323, https://doi.org/10.1007/s11468-023-01852-7.
[18] A.M. Mostafa, S.A. Yousef, W.H. Eisa, M.A. Ewaida, E.A. Al-Ashkar, Au@CdO core/shell nanoparticles synthesized by pulsed laser ablation in Au precursor solution, Appl. Phys. A 123 (2017) 253847739. , https://api.semanticscholar.org/CorpusID:253847739.
[19] M.T. Twafeeq, F.A. Mutlak, Ag/TiO_2 core/shell NPs synthesized by laser ablation and its antibacterial activity, Tikrit J. Pure Sci. 26 (2021) 78–90, https://doi.org/10.25130/tjps.v26i6.196.
[20] M.S.A. Galil, M. Al-qubati, S.O. Mohammed, A. Numan, A. A.R. Saeed, E.A.A. Saif, Effect of single and combined (core/shell) biosynthesis of nanoparticles (Ag and ZnO) on their photocatalytic and antimicrobial activities, Kuwait J. Sci. 52 (2025) 100356, https://doi.org/10.1016/j.kjs.2024.100356.
[21] A. Aldalbahi, M.E. El-Naggar, M.K. Ahmed, G. Periyasami, M. Rahaman, A.A. Menazea, Core-shell Au@Se nanoparticles embedded in cellulose acetate/polyvinylidene fluoride scaffold for wound healing, J. Mater. Res. Technol. 9 (2020) 15045–15056, https://doi.org/10.1016/j.jmrt.2020.10.079.
[22] M.F.H. Abd El-Kader, M.T. Elabbasy, A.A. Adeboye, M.G. M. Zeariya, A.A. Menazea, Morphological, structural and antibacterial behavior of eco-friendly of ZnO/TiO_2 nanocomposite synthesized via *Hibiscus* rosa-sinensis extract, J. Mater. Res. Technol. 15 (2021) 2213–2220, https://doi.org/10.1016/j.jmrt.2021.09.048.
[23] S.A. Rasaki, C. Zhao, R. Wang, J. Wang, H. Jiang, M. Yang, Facile synthesis approach for preparation of robust and recyclable Ag/ZnO nanorods with high catalytic activity for 4-nitrophenol reduction, Mater. Res. Bull. 119 (2019) 110536, https://doi.org/10.1016/j.materresbull.2019.110536.
[24] A.M. Mostafa, E.A. Mwafy, A. Toghan, ZnO nanoparticles decorated carbon nanotubes via pulsed laser ablation method for degradation of methylene blue dyes, Colloids Surf. A Physicochem. Eng. Asp. 627 (2021) 127204, https://doi.org/10.1016/j.colsurfa.2021.127204.
[25] A.A. Saeed, Structural and optical properties for ZnO nanoparticles for antibacterial application, Tikrit J. Pure Sci. 30 (2025) 62–70, https://doi.org/10.25130/tjps.v30i1.1779.
[26] R.H. Ahmed, Optical properties of iron oxide thin films prepared by pulsed laser ablation method, Tikrit J. Pure Sci. 26 (2021) 84–88, https://doi.org/10.25130/tjps.v26i3.146.
[27] A.S. Hussien, A.R. Ahmed, Influence of CuO nanoparticles on the structural, optical and thermal properties of CMC-PVP films, J. Nanostruct. 15 (2025) 239–248. https://jns.kashanu.ac.ir/article_114794.html.
[28] S. Nasiri, M. Rabiei, A. Palevicius, G. Janusas, A. Vilkauskas, V. Nutalapati, A. Monshi, Modified Scherrer equation to calculate crystal size by XRD with high accuracy, examples Fe_2O_3, TiO_2 and V_2O_5, Nano Trends 3 (2023) 100015, https://doi.org/10.1016/j.nwnano.2023.100015.
[29] C.F. Holder, R.E. Schaak, Tutorial on powder x-ray diffraction for characterizing nanoscale materials, ACS Nano 13 (2019) 7359–7365, https://doi.org/10.1021/acsnano.9b05157.
[30] A.B. Rather, T.U. Wani, R.S. Khan, A. Abdal-hay, S.U. Rather, J. Macossay, F.A. Sheikh, Recent progress in the green fabrication of cadmium sulfide and cadmium oxide nanoparticles: synthesis, antimicrobial and cytotoxic studies, Mater. Sci. Eng. B 286 (2022) 116022, https://doi.org/10.1016/j.mseb.2022.116022.
[31] H.H. Nguyen, J. Park, S. Kang, M. Kim, Surface plasmon resonance: a versatile technique for biosensor applications, Sensors 15 (2015) 10481–10510, https://doi.org/10.3390/s150510481.
[32] L. Wang, M.H. Kafshgari, M. Meunier, Optical properties and applications of plasmonic-metal nanoparticles, Adv. Funct. Mater. 30 (2020) 2005400, https://doi.org/10.1002/adfm.202005400.
[33] R. Singhal, M. Fernando, P.K. LeMaire, B. Wu, Characterization of ZnO and Fe doped ZnO nanoparticles using fluorescence spectroscopy, in: Proc. SPIE 10919, Oxide-Based Materials and Devices X, 10919, 2019, https://doi.org/10.1117/12.2510983, 109192P.
[34] N.S. Diab, H.M. Ragab, R.A. Aziz, E.A.A. Elneim, A.M. Alghamdi, S. Naji, M.O. Farea, Synthesis and characterization of PVA/PEO-MWCNT/TiO_2 nanocomposites: enhancements in structural, optical, and antibacterial properties, J. Inorg. Organomet. Polym. Mater. 35 (2025) 3490–3504, https://doi.org/10.1007/s10904-024-03471-z.
[35] F.H. Alkallas, S.M. Alghamdi, E.A. Rashed, A.B.G. Trabelsi, S.S. Nafee, W.B. Elsharkawy, E. Alsubhe, S.H. Alshreef, A. M. Mostafa, Nanocomposite Fe_3O_4-MWCNTs based on femtosecond pulsed laser ablation for catalytic degradation, Diam. Relat. Mater. 140 (2023) 110445, https://doi.org/10.1016/j.diamond.2023.110445.
[36] R. Khalil, N.A. Kelany, M.A. Ibrahim, G.M. Al-Senani, A.M. Mostafa, Linear and nonlinear optical properties of PVA:SA blend reinforced by TiO_2 nanoparticles prepared by flower extract of aloe vera for optoelectronic applications, Coatings 13 (2023) 699, https://doi.org/10.3390/coatings13040699.
[37] Y. Zare, Study of nanoparticles aggregation/agglomeration in polymer particulate nanocomposites by mechanical properties, Compos. Appl. Sci. Manuf. 84 (2016) 158–164, https://doi.org/10.1016/j.compositesa.2016.01.020.
[38] B.H. Kenzaoui, M. Ceridono, P. Urbán, A. Bogni, J. Ponti, S. Gioria, A.K. Ovaskainen, The agglomeration state of nanoparticles can influence the mechanism of their cellular internalisation, J. Nanobiotechnol. 15 (2017) 48, https://doi.org/10.1186/s12951-017-0281-6.
[39] N.K. Abdalameer, K.A. Khalaph, E.M. Ali, Ag/AgO nanoparticles: green synthesis and investigation of their bacterial inhibition effects, Mater. Today Proc. 45 (2021) 5788–5792, https://doi.org/10.1016/j.matpr.2021.03.166.
[40] H.F. Hetta, Y.N. Ramadan, A.I. Al-Harbi, A.E. Ahmed, B. Battah, N.H. Abd-Ellah, S. Zanetti, M.G. Donadu, Nanotechnology as a promising approach to combat multidrug resistant bacteria: a comprehensive review and future perspectives, Biomed. 11 (2023) 413, https://doi.org/10.3390/biomedicines11020413.
[41] D.M. Cruz, E. Mostafavi, A. Vernet-Crua, H. Barabadi, V. Shah, J.L. Cholula-Díaz, G. Guisbiers, T.J. Webster, Green nanotechnology-based zinc oxide (ZnO) nanomaterials for biomedical applications: a review, J. Phys.: Materials (IOP Publishing) 3 (2020) 034005, https://doi.org/10.1088/2515-7639/ab8186.
[42] Z. Yi, X. Yang, Y. Liang, F. Chapelin, S. Tong, Enhancing ROS-inducing nanozyme through intraparticle electron transport, Small 20 (2024) e2305974, https://doi.org/10.1002/smll.202305974.